Gravity- and temperature-driven phase transitions in a model for collapsed axionic condensates

Sanjay Shukla,[1,*] Akhilesh Kumar Verma,[2,†] Marc E. Brachet,[3,‡] and Rahul Pandit[1,§]

[1]*Centre for Condensed Matter Theory, Department of Physics, Indian Institute of Science, Bangalore 560012, India*

[2]*Civil and Architectural Engineering, University of Miami, Coral Gables, Florida 33146, USA*

[3]*Laboratoire de Physique de l'École Normale Supérieure, ENS, Université PSL, CNRS, Sorbonne Université Université de Paris, 24 Rue Lhomond, 75005 Paris, France*

(Received 2 November 2023; accepted 13 February 2024; published 7 March 2024)

We show how to use the cubic-quintic Gross-Pitaevskii-Poisson equation (cq-GPPE) and the cubic-quintic stochastic Ginzburg-Landau-Poisson equation (cq-SGLPE) to investigate the gravitational collapse of a tenuous axionic gas into a collapsed axionic condensate for both zero and finite temperature T. At $T = 0$, we use a Gaussian Ansatz for a spherically symmetric density to obtain parameter regimes in which we might expect to find compact axionic condensates. We then go beyond this Ansatz, by using the cq-SGLPE to investigate the dependence of the axionic condensate on the gravitational strength G at $T = 0$. We demonstrate that, as G increases, the equilibrium configuration goes from a tenuous axionic gas, to flat sheets or *Zeldovich pancakes*, cylindrical structures, and finally a spherical axionic condensate. By varying G, we show that there are first-order phase transitions, as the system goes from one of these structures to the next one; we find hysteresis loops that are associated with these transitions. We examine these states and the transitions between these states via the Fourier truncated cq-GPPE; and we also obtain the thermalized $T > 0$ states from the cq-SGLPE; the transitions between these states yield thermally driven first-order phase transitions and their associated hysteresis loops. Finally, we discuss how our cq-GPPE approach can be used to follow the spatiotemporal evolution of a rotating axionic condensate and also a rotating binary-axionic-condensate system; in particular, we demonstrate, in the former, the emergence of vortices at large angular speeds Ω and, in the latter, the rich dynamics of the mergers of the components of this binary system, which can yield vortices in the process of merging.

DOI: 10.1103/PhysRevD.109.063009

I. INTRODUCTION

Dark matter has a rich history [1]; it includes the *dark bodies* discussed by Kelvin [2], the suggestion of *matière obscure* by Poincaré [3], Zwicky's proposal [4,5] of *Dunkler Materie*, inferred via the virial theorem, and the path-breaking studies of Rubin and Ford on the rotation curves of spiral galaxies that provided evidence for dark-matter haloes (DMH) [6–8]. Dark matter now plays a central role in cosmology [1], e.g., in the simple Λ-cold-dark-matter (ΛCDM) model, where Λ is the cosmological constant, and its generalizations [9–13]. Experiments indicate that $\simeq 85\%$ of the matter in the Universe is non-baryonic cold dark matter [14–18]. Weakly interacting massive particles (WIMPS) [18,19] are among the leading dark-matter candidates. Several experiments have been carried out to establish the nature of dark matter; unfortunately, there is still no unambiguous dark-matter candidate [1,20–22]. While such experimental studies continue, it is important to explore theoretically the properties of other dark-matter candidates, such as self-gravitating assemblies of bosons, also called ultralight dark matter (ULDM) (see, e.g., Refs. [23–31]) or axions [32]. We have studied the former, at temperature $T \geq 0$, by using the Galerkin-truncated Gross-Pitaevskii-Poisson equation [30,31]; here, we generalize this to study a cubic-quintic Gross-Pitaevskii-Poisson equation [32] that is of relevance to axion stars [33] and axion cosmology [34].

A three-dimensional (3D) system of noninteracting mass-m bosons exhibits a Bose-Einstein condensate (BEC) for $T < T_c = [(2\pi\hbar^2 n^{2/3})/(mk_B)]$, the critical temperature at which the thermal de Broglie wavelength $\lambda_{\rm dB} = [2\pi\hbar^2/mk_BT]^{1/2}$ becomes comparable to the mean interparticle spacing $\sim n^{-1/3}$, where n is the number density of bosons and k_B is the Boltzmann constant. To study a system of weakly interacting bosons we use the Gross-Pitaevskii equation (GPE), in which the BEC is a superfluid.

*shuklasanjay771@gmail.com
†akvermajnusps@gmail.com
‡brachet@phys.ens.fr
§rahul@.iisc.ac.in

To account for a nonrelativistic gravitational interaction between such bosons, we couple the GPE with the Poisson equation, i.e., we employ the Gross-Pitaevskii-Poisson equation (GPPE). The scattering length a of the bosonic atoms leads to a self-interaction between the bosons that can either be repulsive ($a > 0$) or attractive ($a < 0$). In the repulsive case, we use the GPPE with a cubic nonlinearity; the $T = 0$ equilibrium state follows by balancing the gravitational interaction with the repulsive self-interaction and the quantum pressure [24]. For $T > 0$ we have carried out an extensive study of this GPPE, by a Galerkin-truncated pseudospectral method [30,31], to obtain compact objects, which can be threaded by vortices if we include rotation.

For the case of attractive self-interactions $a < 0$, which is directly relevant to axionic systems [33–36], the equilibrium $T = 0$ state is unstable above an extremely low critical mass [27], because the repulsive quantum pressure cannot overcome attractive gravitational and self-interactions. Self-gravitating bosonic systems with $a < 0$ are also interesting because it has been hypothesized [25] that they can accelerate the formation of structures if the system starts from a homogeneous distribution of bosons [37]. It behooves us, therefore, to study such systems theoretically.

To study the spatiotemporal evolution of axion stars, we must use the GPPE with both cubic and quintic nonlinearities; the former is negative (because $a < 0$) and favors the collapse instability mentioned above; the quintic nonlinearity, with a coefficient $g_2 > 0$, controls this instability. The resulting cubic-quintic GPPE (cq-GPPE), has been used, in the absence of gravity, to study (a) the evolution and merging dynamics of bright solitons [38,39] in one dimension (1D) and (b) in three dimensions (3D), without the quintic term, for the collision of bright solitons [40] and their collapse times during collisions; these studies use harmonic traps. With self-gravitation, Ref. [41] has used the GPPE, with only the quintic term, to study the dense phase of BEC dark matter; and Ref. [32] has employed the cq-GPPE to obtain a phase transition between dilute and dense axion matter by using a Gaussian Ansatz at temperature $T = 0$; aside from this study, there are very few investigations of the cq-GPPE, in the context of axionic stars, with negative scattering lengths.

Our study of phases and transitions in the cq-GPPE is the first to go beyond the Gaussian Ansatz and $T = 0$. It leads to important insights into structure formation in self-gravitating axionic matter. We give a qualitative summary of our principal results before we present the details of our work. We first obtain the equilibrium configurations at $T = 0$ and then investigate finite-temperature effects ($T > 0$) by using the Fourier-truncated cq-GPPE and building on our boson-star studies with the GPPE [30,31] that generalise Fourier-truncated investigations of the GPE [42–44]. Furthermore, we obtain the equilibrium configuration, for $T \geq 0$, by using an auxiliary cubic-quintic stochastic Ginzburg-Landau-Poisson equation (cq-SGLPE), the imaginary time ($t \to -it$) version of the cq-GPPE.

If we start with a nearly uniform density, the Fourier-truncated $T = 0$ cq-SGLPE collapses, first along one direction, leading to a structure that is reminiscent of a stack of *Zeldovich pancakes* [45]. As we increase the gravitational strength G, these pancakes transform into cylindrical layers, which finally collapse into a spherical axion star. If we cycle G from low to high values and back, this system displays hysteresis loops, associated with first-order phase transitions between these pancake, cylindrical, and spherical states; these loops are examples of *cosmological hysteresis* [46]. We next investigate finite-temperature ($T > 0$): we demonstrate that these collapsed axionic states transform to tenuous, noncollapsed states at high T. Finally, we impose an angular velocity Ω on these states; we show that, beyond a critical angular velocity, quantum vortices thread the axionic star; this critical angular velocity depends on the coefficient g_2 of the quintic nonlinearity. Finally, we employ our cq-GPPE approach to follow the spatiotemporal evolution of a rotating axionic condensate and also a rotating binary-axionic-condensate system; in the former, we show the emergence of vortices at large angular speeds Ω; and, in the latter, we elucidate the rich dynamics of the mergers of the components of this binary system.

The remainder of this paper is organized as follows: In Sec. II we describe the cq-GPPE and cq-SGLPE models and the pseudospectral methods that we use to study these. We present our results in Sec. III. Section IV contains our conclusions and a discussion of the significance of our results.

II. MODEL AND NUMERICAL SIMULATION

We define below the models we use and the numerical methods that we employ to study them.

A. The cq-GPPE and cq-SGLPE

At low temperatures, 3D bosonic systems form a Bose-Einstein condensate (BEC), which can be described by a macroscopic complex wave function $\psi(\mathbf{x}, t)$. For weakly interacting bosons, we can use the GPE; and, in the presence of Newtonian gravity, this can be generalized to the GPPE (see, e.g., Refs. [30,31]). For attractive self interactions between the bosons, as in axionic systems [33,34], we must include a quintic nonlinearity for stability and employ the following cq-GPPE:

$$i\hbar\frac{\partial\psi}{\partial t} = -\frac{\hbar^2}{2m}\nabla^2\psi + [G\Phi + g|\psi|^2 + g_2|\psi|^4]\psi,$$
$$\nabla^2\Phi = |\psi|^2 - \langle|\psi|^2\rangle, \tag{1}$$

m and $n = |\psi|^2$ are, respectively, the mass and number density of bosons, Φ is the gravitational potential,

$G \equiv 4\pi G_N m^2$, and $g \equiv 4\pi a\hbar^2/m$, with $a < 0$ the s-wave scattering length, and $g_2 > 0$ the coefficient of the quintic term. If we linearize Eq. (1) about the constant density $|\psi|^2 = n_0$, we get the dispersion relation, between the frequency ω and the wave number k,

$$\omega(k) = \sqrt{\frac{\hbar^2 k^4}{(2m)^2} - \frac{k^2}{m}\left(\frac{Gn_0}{k^2} - gn_0 - 2g_2 n_0^2\right)}, \quad (2)$$

whence we define the wave number

$$k_J^2 = \frac{2m(gn_0 + 2g_2 n_0^2)}{\hbar^2}\left[-1 + \sqrt{1 + \frac{G\hbar^2 n_0}{m(gn_0 + 2g_2 n_0^2)^2}}\right] \quad (3)$$

below which the low-k Jeans instability occurs.

Equation (1) conserves the number of particles $N \equiv \int |\psi|^2 d^3\mathbf{x}$ and the total energy $E \equiv E_k + E_{\rm int} + E_G$:

$$E = \int \left[\frac{\hbar^2}{2m}|\nabla\psi|^2 + \mathcal{V}(\psi) + \frac{G}{2}|\psi|^2\nabla^{-2}|\psi|^2\right] d^3\mathbf{x},$$
$$\mathcal{V}(\psi) \equiv \frac{g}{2}|\psi|^4 + \frac{g_2}{3}|\psi|^6. \quad (4)$$

In the absence of gravity [$G = 0$], the stationary solution of Eq. (1) in a volume V, has a constant density $|\psi_0|^2 = n_0 = \rho_0/m$, total energy E_0 [Eq. (4)], pressure P_0, and speed of sound v:

$$E_0 = \frac{1}{2}g|\psi_0|^4 V + \frac{1}{3}g_2|\psi_0|^6 V = \frac{1}{2}\frac{gN_0^2}{V} + \frac{1}{3}\frac{g_2 N_0^3}{V^2},$$
$$P_0 \equiv -\frac{\partial E_0}{\partial V} = \frac{1}{2}\frac{g\rho_0^2}{m^2} + \frac{2}{3}\frac{g_2\rho_0^3}{m^3},$$
$$v \equiv \sqrt{\frac{\partial P_0}{\partial \rho_0}} = \sqrt{\frac{gn_0 + 2g_2 n_0^2}{m}}. \quad (5)$$

If we make the approximation $\nabla^2\psi \simeq \psi/\xi^2$, then we can estimate the coherence length ξ by equating the kinetic and interaction terms as follows:

$$\frac{\hbar^2}{2m}\frac{\psi}{\xi^2} = g|\psi|^2\psi + g_2|\psi|^4\psi, \quad \text{whence}$$
$$\xi = \frac{\hbar}{\sqrt{2m(gn_0 + g_2 n_0^2)}}. \quad (6)$$

We use $\tau \equiv \xi/v$ to nondimensionalise the time t in our direct numerical simulations (DNSs). The timescale based on τ and length L of the simulation box are not comparable to the scales used in astrophysics. We define length, time, and mass scales relevant to astrophysics in the Appendix.

We use pseudospectral DNSs to solve the 3D cq-GPPE and cq-SGLPE, in a cubical domain, with side $L = 2\pi$ and N^3 collocation points, and periodic boundary conditions in all three spatial directions. We employ the Fourier expansion

$$\psi(\mathbf{x}) = \sum_{\mathbf{k}} \hat{\psi}_{\mathbf{k}} \exp(i\mathbf{k}\cdot\mathbf{x}), \quad (7)$$

and the 2/3-rule for dealiasing, i.e., we truncate the Fourier modes by setting $\hat{\psi} \equiv 0$ for $|\mathbf{k}| > k_{\rm max}$ [47,48], with $k_{\rm max} = [N/3]$. The Fourier-truncated cq-GPPE is

$$i\hbar\frac{\partial\psi}{\partial t} = P_G\left[-\frac{\hbar^2}{2m}\nabla^2\psi + P_G\{(G\nabla^{-2} + g + g_2 P_G(|\psi|^2))|\psi|^2\}\psi\right], \quad (8)$$

where P_G is the Galerkin projector [with $P_G[\hat{\psi}_{\mathbf{k}}] = \theta(k_{\rm max} - |\mathbf{k}|)\hat{\psi}_{\mathbf{k}}$]. For time marching we use the fourth-order Runge-Kutta scheme RK4.

The total energy $E \equiv E_k + E_{\rm int} + E_G$ now becomes

$$E_k = \frac{\hbar^2}{2m}\int d^3\mathbf{x}|\nabla\psi|^2,$$
$$E_{\rm int} = \int d^3\mathbf{x}\left[\frac{g}{2}(P_G|\psi|^2)^2 + \frac{g_2}{3}\left[P_G\{(P_G|\psi|^2)^2\}\right]|\psi|^2\right],$$
$$E_G = \frac{G}{2}\int d^3\mathbf{x}[P_G|\psi|^2]\nabla^{-2}[P_G|\psi|^2]. \quad (9)$$

Equilibrium configurations of the cq-GPPE can be obtained efficiently by using the following Galerkin-truncated cq-SGLPE, which follows from Eq. (8) via the Wick rotation $t \to -it$:

$$\hbar\frac{\partial\psi}{\partial t} = P_G\left[\frac{\hbar^2}{2m}\nabla^2\psi + \mu\psi - P_G\left[\{G\nabla^{-2} + g + g_2 P_G(|\psi|^2)\}|\psi|^2\right]\psi\right] + \sqrt{\frac{2\hbar}{\beta}}P_G[\xi(\mathbf{x},t)], \quad (10)$$

where μ is the chemical potential, $\beta = 1/(k_B T)$, k_B is the Boltzmann constant, T is the temperature, and $\xi(\mathbf{x},t)$ is a zero-mean Gaussian white noise with $\langle\xi(\mathbf{x},t)\xi^*(\mathbf{x}',t')\rangle = \delta(t-t')\delta(\mathbf{x}-\mathbf{x}')$. Although the truncated cq-SGLPE Eq. (10) does not conserve the total energy, its DNS converges more rapidly to the long-time solution of the truncated cq-GPPE (8) than does a direct DNS of the latter (cf., Refs. [30,49] for the GPPE and the GPE).

B. cq-GPPE with rotation ($\Omega \neq 0$)

One of the most remarkable features of superfluids, rotating with an angular frequency Ω, is the formation of quantized vortices when $\Omega > \Omega_c$, a critical angular

frequency. The circulation around the vortex line is quantized:

$$\oint_C \mathbf{v}_s \cdot \mathbf{dl} = n\kappa, \tag{11}$$

where $\mathbf{v}_s$ is the superfluid velocity, n is an integer, and $\kappa \equiv h/m$. We investigate the formation of quantized vortices in gravitationally collapsed axionic condensates by introducing the rotation term $-\Omega L_z\psi$ into the cq-GPPE (1), where $L_z = -i\hbar(x\partial_y - y\partial_x)$ is the z-component of the angular momentum $\mathbf{L} = \mathbf{x} \times \mathbf{P}$. The equilibrium configuration can then be obtained by using the following cq-SGLPE with the rotation term:

$$\hbar\frac{\partial\psi}{\partial t} = \frac{\hbar^2}{2m}\nabla^2\psi - \left[G\Phi + g|\psi|^2 + g_2|\psi|^4 - \Omega L_z\right]\psi. \tag{12}$$

We first obtain a spherical collapsed condensate by using Eq. (12) for $\Omega = 0$; we then increase Ω slowly up until the critical angular speed Ω_c, beyond which vortices thread the system. In our DNSs with $\Omega \neq 0$, we use the pseudospectral methods that we have described above.

In the remaining part of this paper, we work with the dimensional form of these equations where $\hbar = 1$ and $m = 1$. [In the Appendix, we give the length and times scales that we should use for different astrophysical systems.] We characterise the equilibrium configuration by the scaled radius of gyration:

$$\frac{R}{L} = \frac{1}{L}\sqrt{\frac{\int \rho(r) r^2 d\mathbf{r}}{\int \rho(r) d\mathbf{r}}}. \tag{13}$$

For axions of mass m, the values of g and g_2 in the potential energy Eq. (4) depend on the mass m and the decay constant f. We calculate f in terms of the Planck mass $M_p = (\frac{\hbar c}{G_N})^{1/2}$ (as in Ref. [32]) for the values of g we consider for structure formation and the generation of vortices. If we keep only the first two terms in Eq. (32) of Ref. [32], the instantonic potential of axions is

$$\mathcal{V} = -\frac{\hbar^3 c^3}{16 f^2}|\psi|^4 + \frac{\hbar^6 c^4}{288 f^4 m}|\psi|^6, \tag{14}$$

our definition of $|\psi|^2$ differs from that of Ref. [32] by a factor m. By comparing the first term of the above instantonic potential with the potential in Eq. (4), we have $f^2 = \frac{\hbar^3 c^3}{8|g|}$. In terms of the Planck mass M_p

$$\frac{f}{M_p c^2} = \frac{\hbar}{mc}\sqrt{\frac{G}{32\pi|g|}}. \tag{15}$$

We use $\hbar = 1$, $m = 1$, $g = -15$, $G = 100$, and speed of light c (for units of length and mass see the Appendix), so we have $f \sim 10^{-7} M_p c^2$. Thus, $f \ll M_p c^2$, which is the strong-self-interaction case within the Newtonian limit in Ref. [32] for axions of mass $m \sim 10^{-4}$ eV$/c^2$.

The parameters g and g_2 are not dimensionless. We have $g = 4\pi a\hbar^2/m$ [dimensions of $[M][L]^5[T]^{-2}$]. The parameter $g_2 = \frac{32\hbar^4\pi^2 a^2}{3m^3c^2}$ [dimensions of $[M][L]^8[T]^{-2}$] is obtained by comparing the potential in Eq. (4) with the second term of Eq. (14). In the remainder of this paper, we choose the values of g and g_2 with $\hbar = 1$, $m = 1$, and in terms of the above-mentioned dimensions of $[M]$, $[L]$, and $[T]$; their dimensionless ratio is $\delta \equiv \frac{g_2}{\xi^3 g} = \frac{16\pi}{3}(\frac{c_s}{c})^2(\frac{a}{\xi})$. The values of the ratios c_s/c (ratio of speed of sound to that of light) and a/ξ (ratio of scattering and coherence lengths) are restricted because of computational limitations. We choose δ such that we get a stable collapsed object. [For the units of g and g_2 see the Appendix.]

C. Initial conditions

We use the following initial conditions in our DNSs:

(i) **IC1**: To study the formation of different structures, we solve the cq-SGLPE (10) at $T = 0$, with an initially uniform density on which we superimpose a small nonuniform perturbation.

(ii) **IC2**: After we obtain a stable axionic condensate, we study the collision dynamics of two such condensates by using Eq. (8) and the following initial condition for this binary system [cf., Ref. [50]]: We first obtain a radially symmetric solution $\psi(r,t)$ via the expansion

$$\psi(r,t) = \sum_{n=0}^{N_R/2} \hat{\psi}_{2n}(t) T_{2n}(r/R'), \tag{16}$$

where T_n is the order-n Chebyshev polynomial (of the first kind) and $\hat{\psi}_{N_{R'}}$ is chosen to satisfy the boundary condition $\psi(R',t) = 0$. We then use the following relaxation method to obtain the stationary state of Eq. (1):

$$\psi(r,t+dt) = \Theta^{-1}\left[\psi(r,t) - dt\left\{(G\Phi + g|\psi|^2 + g_2|\psi|^4)\psi\right\}\right], \tag{17}$$

where $\Theta = 1 - dt\nabla^2|_r/2$ and $\nabla^2|_r \equiv \frac{1}{r^2}\frac{\partial}{\partial r}(r^2\frac{\partial}{\partial r})$. For rapid convergence to the stationary state, we use the following Newton method: We define $f_j(\psi) \equiv \psi_j(t+dt) - \psi_j(t)$ and look for the root ψ_{j*} at which $f_j(\psi_{j*}) = 0$; here, $\psi_j(t)$ is the value of $\psi(t)$ at the collocation point j. At every Newton iteration step, we solve (numerically) $\sum_k[(df_j/d\psi_k)\delta\psi_k] = -f_j(\psi_j)$, to find $\delta\psi_k$ [51].

III. RESULTS

We present our results as follows: In Sec. III A we present analytical results that use a Gaussian Ansatz for a spherically symmetric density profile. Sections III B and III C are devoted, respectively, to our studies at temperature $T = 0$ and $T > 0$. In Secs. III D and III E we discuss, respectively, a rotating axionic condensate and a rotating binary-axionic-condensate system.

A. The Gaussian Ansatz

Most analytical treatments of the cq-GPPE make the following Gaussian approximation for a spherically symmetric density profile (see, e.g., Ref. [24]):

$$\rho(r) = \rho(0) e^{-r^2/R^2_{\rm Gauss}}, \tag{18}$$

where $\rho(0) = M/(\pi^{3/2} R^3_{\rm Gauss})$ is the central density, and $R_{\rm Gauss}$ is the radius of the axionic collapsed object in this approximation. We contrast, in Fig. 1, illustrative density profiles of spherically collapsed axion stars, which we obtain from this Gaussian Ansatz and our DNSs of Eq. (10), for various values of g_2, but with fixed $g = -0.01$ and $G = 1$. We find that this Ansatz approximates the density profiles very well for small g_2 [see Fig. 1(a)]. As g_2 increases [see Figs. 1(b) and 1(c)], the DNS density profile approaches that of a polytrope of index $n = 1/2$, which has a compact support [24], and the Gaussian Ansatz becomes a poor approximation.

If we continue with this simple Gaussian Ansatz, we can calculate the effective-potential-energy curve, whose minimum yields the collapsed axion star, as follows. By using the Madelung transformation

$$\psi(\mathbf{r}, t) = \sqrt{\frac{\rho}{m}} e^{i\vartheta(\mathbf{r},t)} \tag{19}$$

we rewrite the different parts of the total energy Eq. (4) as

$$\begin{aligned} E_k &= \frac{1}{2}\int \rho \mathbf{v}_s^2 d^3\mathbf{x} + \frac{\hbar^2}{8m^2}\int \frac{(\nabla\rho)^2}{\rho} d^3\mathbf{x}, \\ E_{\rm int} &= \int \left(\frac{g}{2m^2}\rho^2 + \frac{g_2}{3m^3}\rho^3\right) d^3\mathbf{x}, \\ E_G &= \frac{G}{2}\int \rho\Phi d^3\mathbf{x}, \end{aligned} \tag{20}$$

where $\mathbf{v}_s = \frac{\hbar}{m}\nabla\vartheta$ and the gravitational potential is calculated via $\Phi = \int \frac{\rho(\mathbf{x}')}{|\mathbf{x}-\mathbf{x}'|} d^3\mathbf{x}'$. The kinetic energy E_k is a sum of the classical E_{kc} and quantum E_{kq} kinetic energies:

$$\begin{aligned} E_{kc} &= \frac{1}{2}\int \rho \mathbf{v}_s^2 d^3\mathbf{x}, \\ E_{kq} &= \frac{\hbar^2}{8m^2}\int \frac{(\nabla\rho)^2}{\rho} d^3\mathbf{x}. \end{aligned} \tag{21}$$

Given the Gaussian Ansatz (18), we can calculate these energies (by performing different integrals via *Mathematica*) to obtain

$$\begin{aligned} E_{kq} &= \frac{3\hbar^2 M}{4m^2 R^2_{\rm Gauss}}, \\ E_{\rm int} &= \frac{g_2 M^3}{9\sqrt{3}m^3\pi^3 R^6_{\rm Gauss}} + \frac{gM^2}{4\sqrt{2}m^2\pi^{3/2}R^3_{\rm Gauss}}, \\ E_G &= -\frac{GM^2}{4\pi\sqrt{2\pi}m^2 R_{\rm Gauss}}, \end{aligned} \tag{22}$$

whence we get

$$E = E_{kc} + \mathcal{V}_{\rm eff}, \tag{23}$$

where the effective potential is

$$\mathcal{V}_{\rm eff} = E_{kq} + E_{\rm int} + E_G. \tag{24}$$

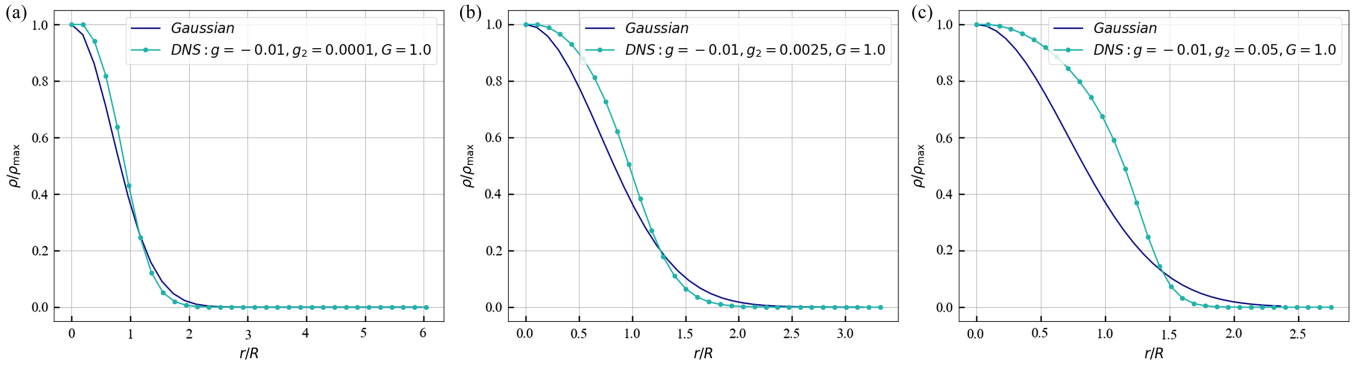

FIG. 1. Plots of the density $\rho(r)/\rho_{\rm max}$ versus r/R, the scaled distance from the center of the axion star, for different values of the parameters g, g_2, and G. The light blue curve is from our DNS and the dark blue curve follows from the Guassian Ansatz [see the text and Eq. (18)]. R is the radius of gyration given in Eq. (13).

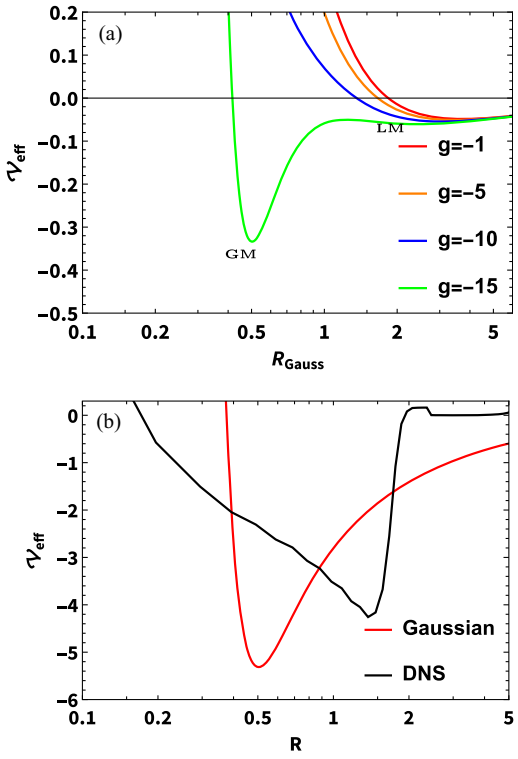

FIG. 2. (a) Log linear plots of the effective potential $\mathcal{V}_{\rm eff}$ versus the axionic condensate's radius $R_{\rm Gauss}$ [see Eq. (18)], for $g_2 = 8$, $G = 14$, and $M = 0.97$. The minima labeled **LM** and **GM** correspond, respectively, to low- and high-density phases of axionic condensates. (b) Plots of $\mathcal{V}_{\rm eff}$ versus the radius of gyration R [Eq. (13)], for $g = -15$, $g_2 = 8$, $G = 100$, and $M = 0.97$, obtained by using the Gaussian Ansatz (in red) and our DNS (in black).

In Fig. 2(a) we present plots of $\mathcal{V}_{\rm eff}$ versus $R_{\rm Gauss}$, for $g_2 = 8$, $G = 14$, $M = 0.97$, and different values of the attraction parameter g, to show that there is a single, low-density minimum at small negative values of g. As we increase the attraction, a new minimum appears: At large negative values of g, there are two minima, labeled **LM** and **GM**, which correspond, respectively, to low- and high-density phases of the axionic system; e.g., at $g = -15$, the dense axionic condensate is the global minimum **GM** of $\mathcal{V}_{\rm eff}$. We also calculate $\mathcal{V}_{\rm eff}$ by using our DNS of Eq. (10) and compare it with the Gaussian-Ansatz effective potential of Eq. (24). In Fig. 2(b), we present plots of $\mathcal{V}_{\rm eff}$ versus the radius of gyration R from our DNS (in black) and the Gaussian Ansatz (in red), for $g = -15$, $g_2 = 8$, $G = 100$, and $M = 0.97$. Although the Gaussian Ansatz does not yield quantitatively accurate positions of minima of $\mathcal{V}_{\rm eff}$, for $g = -15$, $g_2 = 8$, it shows the existence of a stable axionic condensate. [To compare our DNS results with their Gaussian-Ansatz counterparts, we must account for the following factor: $R_{\rm Gauss} = \sqrt{2/3}R$, with R the radius of gyration [Eq. (13)].

B. Collapsed axionic condensates: $T = 0$

Our Gaussian-Ansatz study of $\mathcal{V}_{\rm eff}$ shows that, for $g = -15$ and $g_2 = 8$, a stable axionic condensate may occur. We now investigate the G-dependence of such an axionic condensate by solving the cq-SGLPE (10). We first consider $T = 0$ and start with the initial condition **IC1**, a nearly homogeneous distribution of ψ, and then we increase G from zero to large values. In Fig. 3, we show ten-level contour plots of the spatial variation of $|\psi(\mathbf{x}, t)|^2$, at the initial time (column-1) and final time (column-2) for $G = 0$ [first row of Fig. 3], $G = 4$ [second row of Fig. 3], $G = 34$ [third row of Fig. 3], and $G = 98$ [fourth row of Fig. 3]. The initial conditions for the runs in rows 2, 3, and 4, are, respectively, the final configurations in rows 1, 2, and 3. In each row, the equilibrium configuration (column 2) for a given value of G, is a result of a balance between the self-interactions and the repulsive quantum pressure. Note that, as G increases, the equilibrium configuration goes from a tenuous axionic gas [row 1], to flat sheets [row 2] or *Zeldovich pancakes* [52], cylindrical structures [row 3], and finally a spherical axionic condensate [row 4]. In column 3 of Fig. 3 we illustrate the evolution of the scaled radius of gyration R/L as a function of the scaled time $t/(\xi/v)$ for (a) $G = 0$, (b) $G = 4$, (c) $G = 34$, and (d) $G = 98$. In row 5 we show ten-level contour plots of $|\psi(\mathbf{x}, t)|^2$, with the same parameters as for row 2, but which we obtain by using the cq-GPPE (8).

To study the transitions between the $T = 0$ equilibrium configurations shown in column 2, rows 1–4, in Fig. 3, we increase (blue curve) and then decrease (green curve) G, as we show via the plot of R/L versus G in Fig. 4, for the illustrative values $g = -15$ and $g_2 = 8$ in the cq-GPPE. As we increase G, there are three first-order transitions, first from a statistically homogeneous state to pancakes, then to a cylindrical configuration, and finally to a collapsed spherical object. At the transitions between these configurations, R/L jumps discontinuously. Given that we change the values of G at a finite rate, the metastability of these configurations makes the first-order jumps appear as hysteresis loops [53], in which the increasing-G (blue curve) and decreasing-G (green curve) scans yield different branches. It is interesting to speculate if this is an example of the *cosmological hysteresis* proposed in Ref. [54]: "a universe filled with scalar field exhibits cosmological hysteresis."

C. Formation of axionic objects: $T > 0$

We now study finite-temperature ($T > 0$) effects, on the various structures obtained in Fig. 3, by using the Fourier-truncated cq-GPPE (8); we also construct the thermalized state directly by using the cq-SGLPE (10). Columns 1, 2, and 3 of Fig. 5 show ten-level contour plots of $|\psi(\mathbf{x}, t)|^2$ at different representative temperatures, which increase from

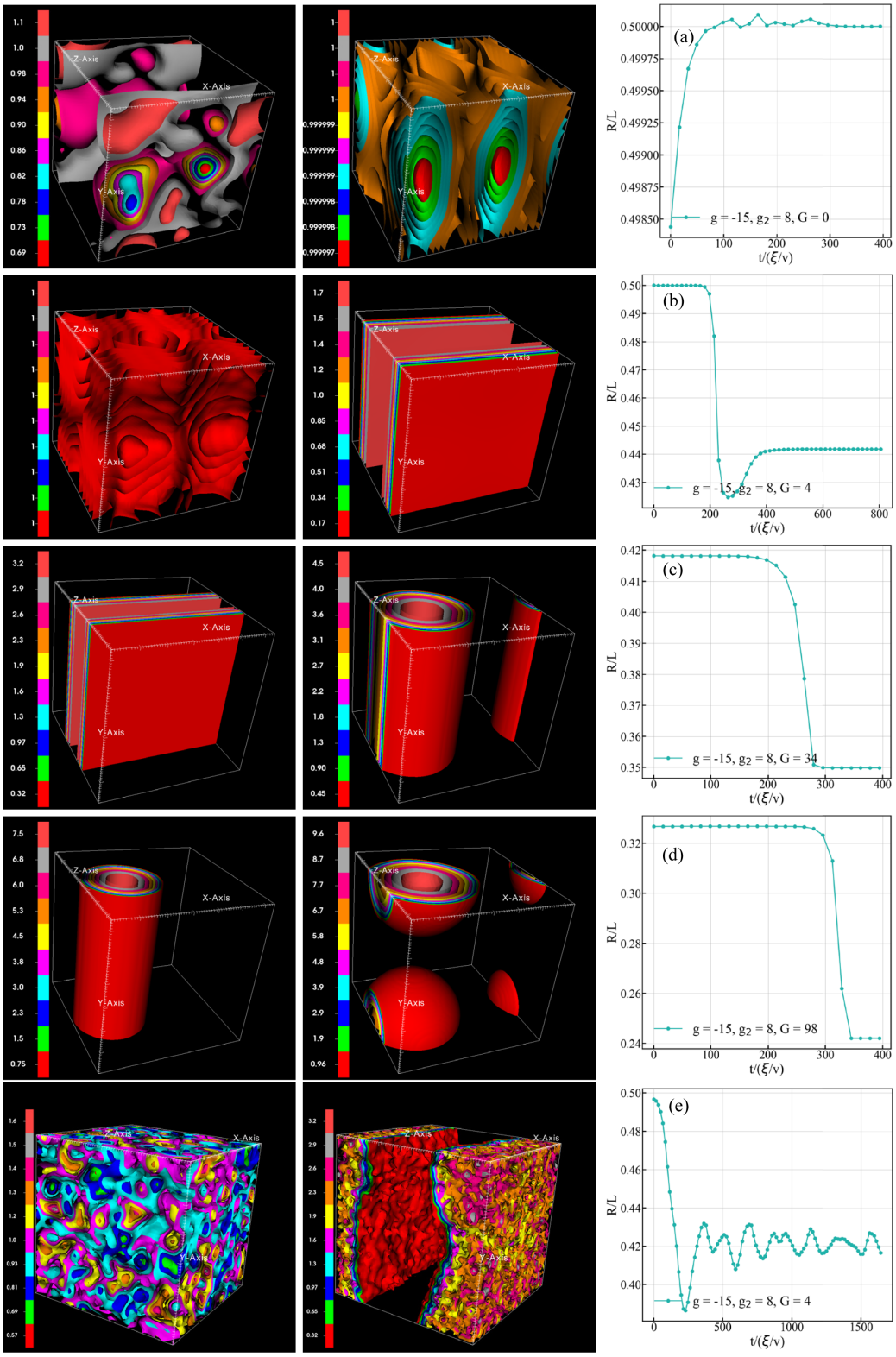

FIG. 3. Ten-level contour plots of $|\psi(\mathbf{x},t)|^2$ from the cq-SGLPE (10) at $T=0$, with initial and final states in columns 1 and 2, respectively, and $G=0$ [first row], $G=4$ [second row], $G=34$ [third row], and $G=98$ [fourth row] and the initial conditions given in the text. Column 3: R/L versus the scaled time $t/(\xi/v)$ for (a) $G=0$, (b) $G=4$, (c) $G=34$, and (d) $G=98$. Row 5 shows the contour plots of $|\psi(\mathbf{x},t)|^2$, for the same parameters as for row 2, but by using the cq-GPPE Eq. (8).

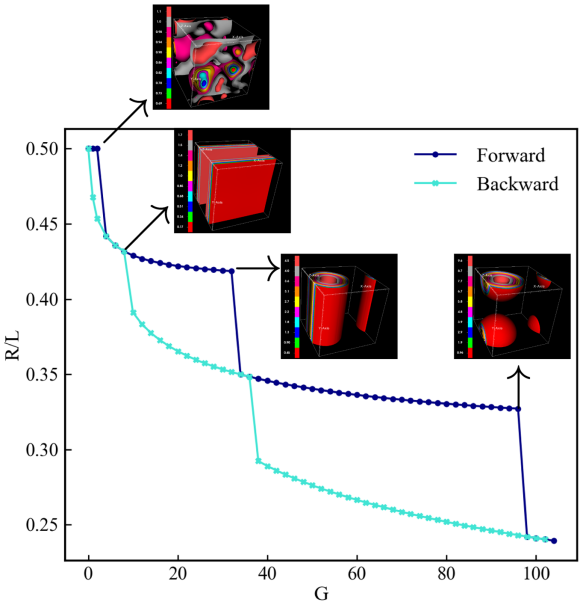

FIG. 4. Plot of the scaled radius of gyration R/L versus the gravitational interaction parameter G for $g = -15$ and $g_2 = 8$ in the cq-GPPE; blue and green curves show, respectively, curves along which G increases and decreases.

column 1 to 3. At $T = 0$ we have pancake, cylindrical, and spherical structures at $G = 30$, $G = 70$, and $G = 104$ in rows 1, 2, and 3, respectively. As we increase T and move from column 1 to 3, we see that, in all the rows, each one of the condensed structures becomes a disordered tenuous axionic assembly. In column 4 of Fig. 5 we show plots of the scaled radius of gyration R/L versus the temperature T. We start with the density distributions illustrated in column 1 of Fig. 5. We then increase T, for each one of these initial conditions; we follow this by a cooling cycle until the system returns to the initial temperature. These heating and cooling cycles yield the hysteresis loops that we show in column 4 of Fig. 5 (with navy blue and cyan lines for heating and cooling cycles, respectively). Although the loops are clearly visible, they are not as pronounced as their counterparts in Fig. 4.

D. Rotational dynamics of a single axionic condensate

Quantized vortices appear when we rotate a superfluid with a sufficiently large angular speed Ω. To obtain such quantized vortices in our self-gravitating system of axions, we solve the cq-SGLPE (12). First we use initial condition **IC1** in Eq. (12), with $\Omega = 0$; for the chosen set of parameters this yields a spherical collapsed object. We now use this collapsed object as the initial condition for Eq. (12) and slowly increase the angular speed Ω. We use the final steady-state value for the field ψ, for a given value of Ω, as the initial condition for the next value of Ω.

In Figs. 6(a)–6(c), we present contour plots of $|\psi(\mathbf{x}, t)|^2$, for a single rotating compact axionic object, with the (z) axis of rotation indicated by a green arrow. We obtain this configuration by solving the cq-SGLPE for $g = -15$, $g_2 = 8$, $G = 100$, and (a) $\Omega = 3$, (b) $\Omega = 4$, and (c) $\Omega = 5$. Note that vortices thread the collapsed object once $\Omega > \Omega_c \gtrsim 3$, where Ω_c is the critical angular speed required for the appearance of vortices. The number density of vortices increases as we increase Ω [cf. Figs. 6(b) and 6(c)]. Furthermore, we show in Fig. 6(d) that Ω_c decreases as g_2 increases. Our result is akin to that of Ref. [55], for a trapped BEC without the G and g_2 terms, where it is found that the critical angular speed decreases as the repulsive interaction g between the bosons increases. For our self-gravitating axionic system, with $g < 0$ and G held fixed, Fig. 6(d) suggests that, as $g_2 \to 0$, the critical angular speed Ω_c becomes so high that the system cannot support vortices.

E. Rotational dynamics of binary axionic systems

We now investigate the dynamics of a rotating binary axionic system by using the following initial condition that consists of two spherical collapsed axionic objects, separated by a distance d, along the y-direction, and with equal and opposite initial velocities, $\mathbf{v_1} = (v, 0, 0)$, $\mathbf{v_2} = (-v, 0, 0)$, in the x-direction:

$$\psi_b(\mathbf{x}, t = 0) = f(|\mathbf{x} - \mathbf{x_0}|)e^{i\mathbf{v_1}\cdot\mathbf{x}} + f(|\mathbf{x} + \mathbf{x_0}|)e^{i(\mathbf{v_2}\cdot\mathbf{x} + \Delta\phi)}, \tag{25}$$

where $\mathbf{x_0} = (0, d/2, 0)$ and $\Delta\phi$ is the relative phase between the two objects. We obtain the function $f(|\mathbf{x}|)$ by using initial condition **IC2** and then the Newton method [cf. the discussion around Eq. (17)], which converges rapidly to the stationary state of the cq-GPPE (1). We explore the dependence of the dynamics of such axionic binaries in the following two illustrative parameter regimes, PI and PII.

1. Parameters PI

We first study the binary system in which the two axionic compact objects have the same mass, $N_1 = N_2 = N/2$, where N is the number of bosons. We evolve Eq. (8) in time, by starting with the initial condition of Eq. (25), $v = 0.5$, and $g = -0.5$, $g_2 = 0.001$, and $G = 2.0$. In the black panel of the first row of Fig. 7, we show isosurface plots of $|\psi(\mathbf{x}, t)|^2$ for the rotating binary system at different representative times and with $\Delta\phi = \pi$. We observe clearly that the two components of the binary system approach each other initially and collide; then they bounce off of each other, but again come close together, albeit with a reduced separation; and finally these components merge after a large time.

In the black panel of the second row of Fig. 7, we show isosurface plots of $|\psi(\mathbf{x}, t)|^2$ for the rotating binary system at different representative times and with $\Delta\phi = 0$, i.e., with

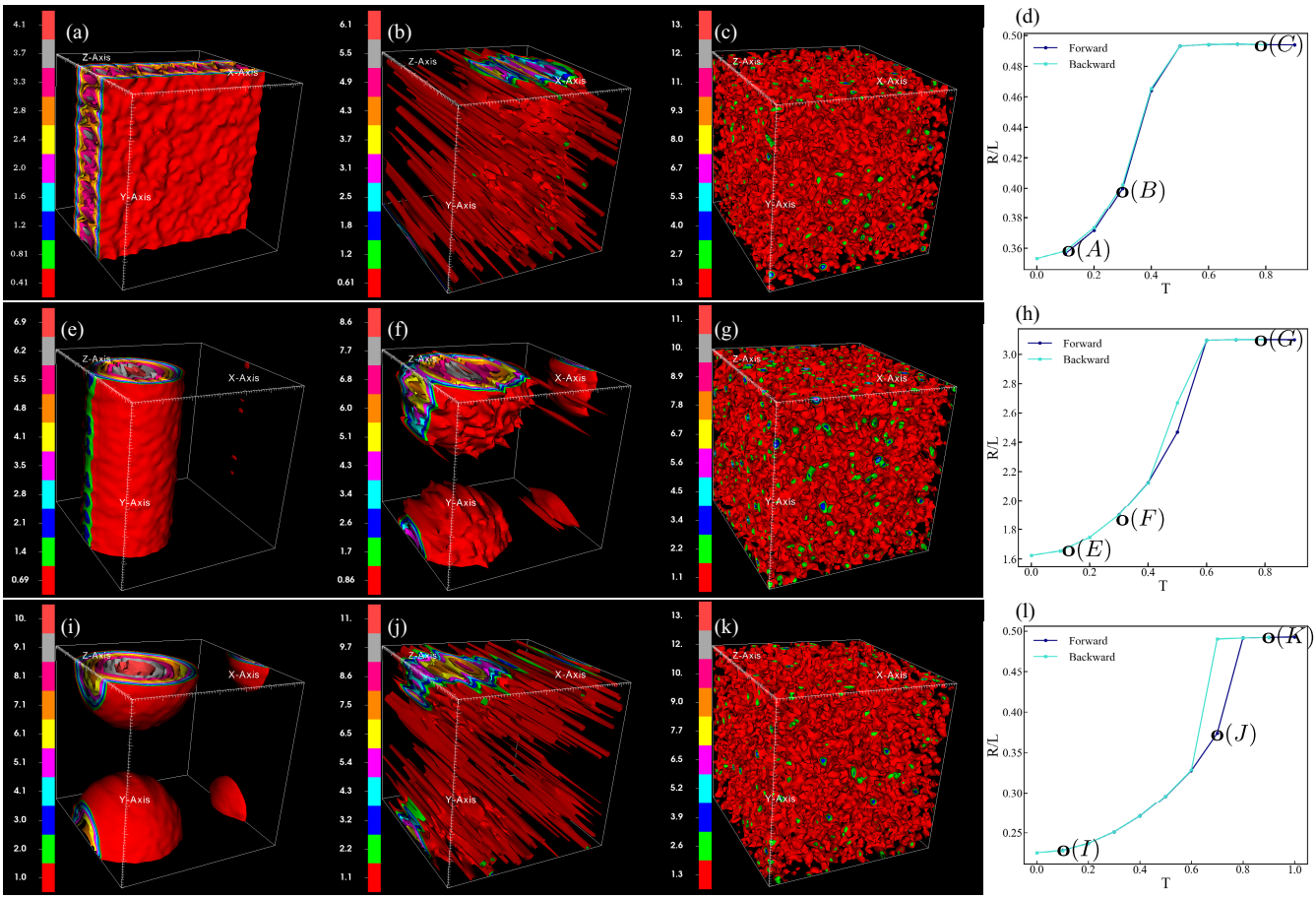

FIG. 5. Columns 1–3: Ten level contour plots of $|\psi(\mathbf{x},t)|^2$ at different temperatures as we heat last snapshots of Fig. 3. The three rows are arranged with increasing value of G; for $G=30$ in row 1, $G=70$ in row 2, and $G=104$ in row 3. Column 4 shows the scaled radius of gyration, R/L vs the temperature T. The black curve is for the heating part of the cycle and the green one is for the cooling part. The points (a)–(c) in (d) corresponds to density distributions in columns 1–3.

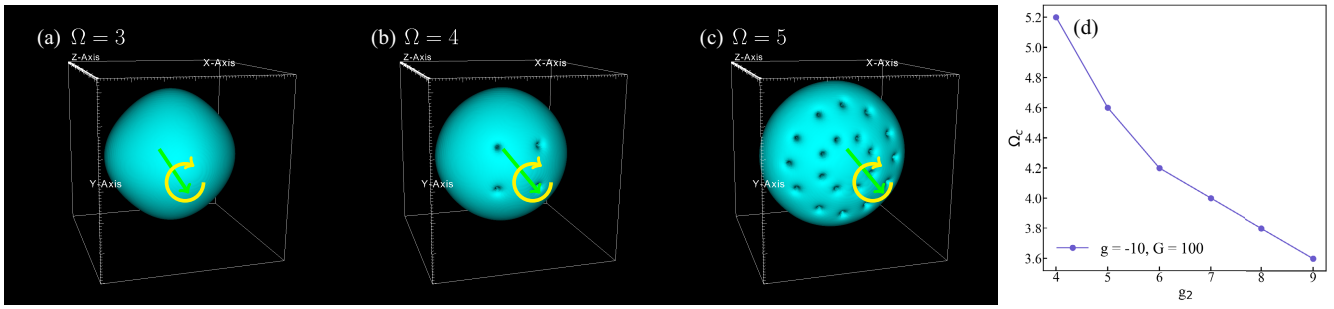

FIG. 6. Contour plots of $|\psi(\mathbf{x},t)|^2$, for a single rotating compact axionic object, which we obtain by solving the cq-SGLPE for $g=-15$, $g_2=8$, $G=100$, and (a) $\Omega=3$, (b) $\Omega=4$, and (c) $\Omega=5$. Vortices appear once $\Omega>\Omega_c$, a critical angular speed. The axis of rotation is indicated by the green arrow (the Z-axis about which the axion condensate is rotated). (d) Plot of Ω_c versus g_2.

the two components of the binary system out of phase. We observe that the collapse of the two components of the binary system occurs in a very short time, compared to the collapse time for $\Delta\phi=\pi$ [cf. the time labels in the black panels of the first and second rows in Fig. 7]. In Fig. 8, we plot versus time t the distance d between the centers of masses of the components of the binary system [Fig. 7], to demonstrate that the collapse of these two components occurs more rapidly for $\Delta\phi=0$ (red curve) than for $\Delta\phi=\pi$ (black curve). The collapse is not monotonic for $\Delta\phi=\pi$ as is clear from the oscillations in the black curve in Fig. 8.

In the last column of Fig. 7, we present plots versus time t of the kinetic energy E_{kq}, the interaction energy $E_{\rm int}$, the

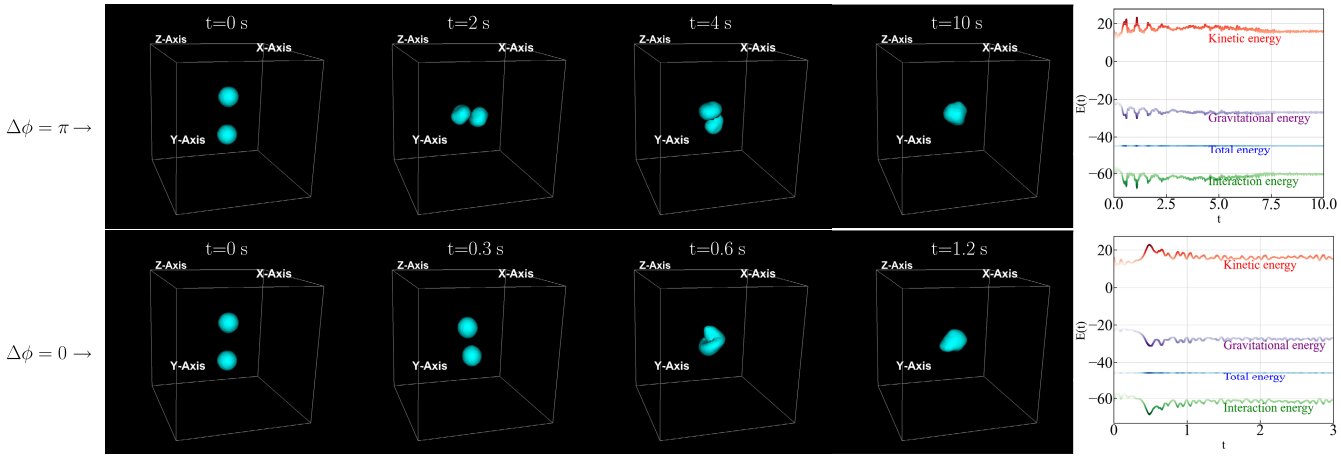

FIG. 7. Contour plots of $|\psi(\mathbf{x}, t)|^2$ for a rotating binary axion system, obtained by using the cq-GPPE for parameter set PI, i.e., $g = -0.5$, $g_2 = 0.001$, $G = 2.0$ and relative phase, $\Delta\phi = \pi$ (top row) and $\Delta\phi = 0$ (bottom row). Plots in the last column show the time evolution of the kinetic, gravitational, interaction, and total energies.

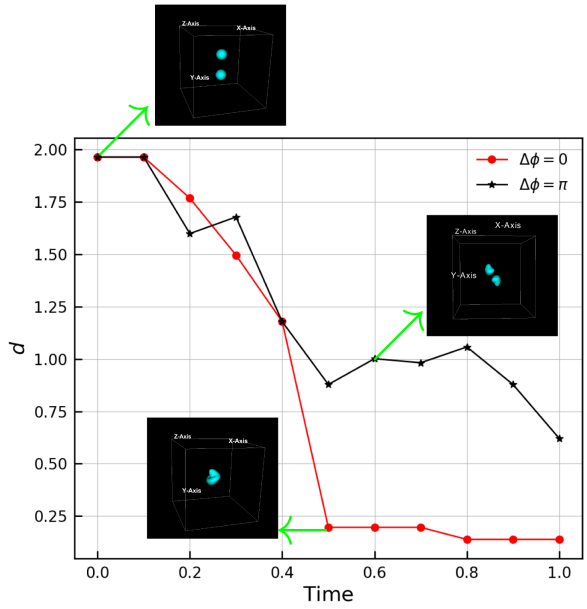

FIG. 8. Plots versus time t the distance d between the centers of masses of the components of the binary system [Fig. 7], to demonstrate that the collapse of these two components occurs more rapidly for $\Delta\phi = 0$ (red curve) than for $\Delta\phi = \pi$ (black curve).

gravitational energy E_G, and the total energy E; the plot in the first (second) row is for $\Delta\phi = \pi$ ($\Delta\phi = 0$). These plots lead to the following important results:

(i) The temporal oscillations in these curves are associated with the bouncing of the two components of the binary system before their eventual merger. The differences in the timescales on the horizontal axes of top and bottom graphs confirm that the collapse of the binary system occurs more rapidly when $\Delta\phi = 0$ than if $\Delta\phi = \pi$.

(ii) The total energy $E < 0$ for both $\Delta\phi = 0$ and $\Delta\phi = \pi$. This is similar to the result of Ref. [56], for the interaction between two BEC halos, which finds that the two halos collide and merge when $E < 0$.

(iii) The rapid merger for $\Delta\phi = 0$ in our cq-GPPE system suggests that there is a well in the potential energy, which favors the formation of a bound state for our binary system. Studies of a rotating-binary system in the conventional Gross-Pitaveskii-Poisson equation (GPPE) with repulsive self interactions, i.e., $g > 0$ [but $g_2 = 0$] also show that the two components merge more easily when they are in-phase than if they are out-of-phase.

2. Parameters PII

Next we investigate the binary system in which the two axionic compact objects have the same mass, $N_1 = N_2 = N/2$, where N is the number of bosons. We evolve Eq. (8) in time, by starting with the initial condition of Eq. (25), $v = 0.5$, and $g = -0.5$, $g_2 = 0.005$, and $G = 2.0$, i.e., the same as the parameter set PI except for a five-fold increase in the axion-interaction strength g_2.

In Fig. 9 we show volume plots of $|\psi(\mathbf{x}, t)|^2$ for the out-of-phase $\Delta\phi = \pi$ (first row) and in-phase $\Delta\phi = 0$ (second row) cases. In this instance too, the two objects merge more quickly in the second case than in the first.

The two compact objects in this binary system have equal and opposite velocities initially. As the system evolves, the two objects merge and the single collapsed object rotates with a finite angular momentum. If this angular momentum is sufficiently high, it is possible to obtain quantized vortices, if the interaction strength g_2 is large. The volume plot in the first row of Fig. 9 clearly shows a vortex. Such a vortex can also be visualized by plotting the density variation along one direction for the last configuration of the collapsed, rotating

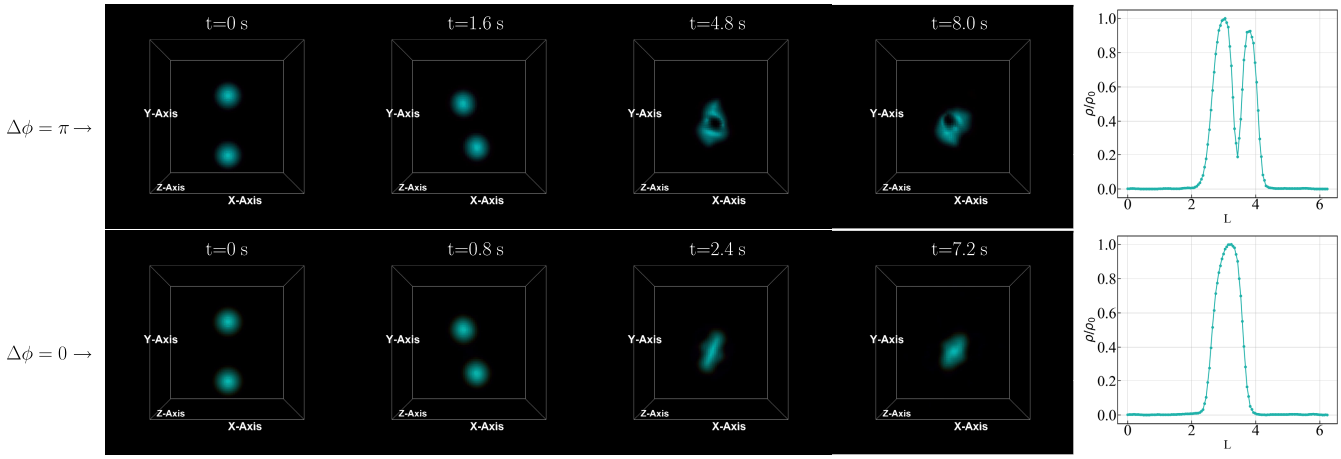

FIG. 9. Volume plots of $|\psi(\mathbf{x}, t)|^2$ for a rotating binary axionic system obtained by using the cq-GPPE for parameter set PII, i.e., $g = -0.5$, $g_2 = 0.005$, $G = 2.0$ and relative phase $\Delta\phi = \pi$ (first row) and $\Delta\phi = 0$ (second row). The last column shows plots of the density variation along the line passing through the center of the last configuration of the collapsed, rotating axionic system.

axionic object. We show such plots in the last column of Fig. 9. The large dip in the density, approximately at the middle, indicates a vortex when $\Delta\phi = \pi$; we do not observe such a dip if $\Delta\phi = 0$.

IV. CONCLUSIONS

We have shown how to use the cq-GPPE (8) and the cq-SGLPE (10) to investigate the gravitational collapse of a tenuous axionic gas into a collapsed axionic condensate for $T \geq 0$. We have first presented analytical results at $T = 0$, which use a Gaussian Ansatz for a spherically symmetric density profile [24] and suggest parameter regimes in which we might expect to find compact axionic condensates. We have gone beyond this Ansatz by using the cq-SGLPE (10) to investigate the G-dependence of the axionic condensate at $T = 0$, and shown that, as G increases, the equilibrium configuration goes from a tenuous axionic gas, to flat sheets or *Zeldovich pancakes* [52], cylindrical structures, and finally a spherical axion condensate [see Fig. 3]. By varying G, we have shown that there are first-order phase transitions as the system goes from one of these structures to the next one, as we see clearly by the hysteresis loops in Fig. 4. We have then examined these states and the transitions between these states via the Fourier truncated cq-GPPE (8) and also by obtaining the thermalized $T > 0$ states [see Fig. 5] from the cq-SGLPE (10); transitions between these states yield thermally driven first-order phase transitions and their associated hysteresis loops. Finally, we have discussed how our cq-GPPE approach can be used to follow the spatiotemporal evolution of a rotating axion condensate and also a rotating binary-axion-condensate system; in particular, we have examined, in the former, the emergence of vortices at large angular speeds Ω and, in the latter, the rich dynamics of the mergers of the components of this binary system, which can yield vortices in the process of merging.

Our work goes beyond earlier studies [30,31,57,58] that use the conventional cubic GPPE, which is appropriate for boson condensates that are not axionic. The latter require the inclusion of the quintic term in the cq-GPPE, which we have studied in detail here. We also note that the cq-GPPE arises naturally in the Taylor expansion of instantonic potentials of axions [32]. In future work we will explore axionic generalizations of Ref. [31] and explore relations, if any, of the emergence of vortices in a recent study of the mergers of black holes and saturons [59]. If dark matter indeed consists of BECs, then dark-matter galactic halos and axionic or bosonic stars should be capable of generating quantized vortices, because of the tidal torques from the surrounding matter as studied; for instance, Refs. [60,61] study the formation and effects of vortices on the rotation curves of spiral galaxies; their results are in agreement with observations obtained from the Andromeda Galaxy and suggest the existence of substructures on these curves, which agree with the observations on some spiral galaxies. Our studies could find applications in such astrophysical settings.

ACKNOWLEDGMENTS

We thank the Indo-French Centre for Applied Mathematics (IFCAM), the Science and Engineering Research Board (SERB), and the National Supercomputing Mission (NSM), India for support, and the Supercomputer Education and Research Centre (IISc) for computational resources.

APPENDIX

We use the dimensionless form of the cubic-quintic Gross-Pitaevskii-Poisson equation (cq-GPPE), which we obtain by setting $\hbar = 1$, and $m = 1$. Here we discuss

the units relevant for different astrophysical settings. For $\hbar = 1$, we have

$$1\frac{([M]kg)\cdot([L]me)^2}{([T]s)} = 1.054\times10^{-34}\frac{me^2\cdot kg}{s}, \quad \text{(A1)}$$

where $[L]$, $[T]$, and $[M]$ are the units of length, time, and mass, respectively, and me represents metre. We now calculate the astrophysically relevant mass and timescales (depending on the object of interest).

(i) If the cq-GPPE (1) describes a dark-matter halo, we consider ultralight axions of mass $m \simeq 10^{-23}$ eV$/c^2$, which fixes the unit of mass. Therefore, choosing $m = 1$ amounts to using

$$1([M]\text{kg}) = 10^{-23}\frac{\text{eV}}{c^2},$$
$$[M] = 1.78\times10^{-59}\text{ kg}. \quad \text{(A2)}$$

By using Eqs. (A1) and (A2) we get

$$[T] = 1.69\times10^{-25}[L]^2 s, \quad \text{(A3)}$$

and we can choose the unit of length to be 1 kpc $\simeq 3\times10^{19}$ m [62]. Therefore, for dark-matter haloes

$$[T] = 1.52\times10^{14}\text{ s} \simeq 4.8\times10^{6}\text{ yr} = 4.8\text{ Myr},$$
$$[M] = 1.78\times10^{-59}\text{ kg}. \quad \text{(A4)}$$

With these units of length $[L]$, mass $[M]$, and time $[T]$ for dark-matter haloes, our simulation box is of size $(2\pi\times2\pi\times2\pi)$ kpc^3 and the time step of 0.000001 is equivalent to $dt = 4.8$ yrs.

(ii) If the cq-GPPE (1) describes an axionic star, we consider axions of mass $m \simeq 10^{-4}$ eV$/c^2$, which fixes the unit of mass. Therefore, choosing $m = 1$ amounts to using

$$1([M]\text{kg}) = 10^{-4}\frac{\text{eV}}{c^2},$$
$$[M] = 1.78\times10^{-40}\text{ kg}. \quad \text{(A5)}$$

By using Eqs. (A1) and (A5) we obtain

$$[T] = 1.69\times10^{-6}[L]^2\text{ s}. \quad \text{(A6)}$$

If we choose the unit of length to be $1[L] = 1$ km then, for axionic stars,

$$[T] = 1.69\text{ s} \quad \text{(A7)}$$

$$[M] = 1.78\times10^{-40}\text{ kg}. \quad \text{(A8)}$$

With these units of length $[L]$, mass $[M]$, and time $[T]$ for axionic stars, our simulation box is of size $(2\pi\times2\pi\times2\pi)$ km^3 and the time step of 0.000001 is equivalent to $dt = 1.69$ μs.

(iii) The coefficient of cubic nonlinearity g is given as follows

$$g = \frac{4\pi a\hbar^2}{m}\frac{kg\cdot me^5}{s^2}, \quad \text{(A9)}$$

where me represents the metre. For axions of mass $m \simeq 10^{-4}$ eV$/c^2$, using Eq. (A8) with $\hbar = m = 1$, we have

$$g = 20.11a\times10^{25}\frac{[M][L]^5}{[T]^2} \quad \text{(A10)}$$

For the ratios a/ξ and c_s/c (based on the computational limits), we choose g and g_2 such that the nondimensional ratio $\delta = \frac{g_2}{\xi^3 g}$ gives a stable collapsed object. Here ξ is the healing length, and c_s is the speed of sound.

[1] G. Bertone and D. Hooper, History of dark matter, Rev. Mod. Phys. **90**, 045002 (2018).
[2] L. W. T. Kelvin, *Baltimore Lectures on Molecular Dynamics and the Wave Theory of Light* (C. J. Clay and Sons, London, 1904).
[3] H. Poincaré, The Milky Way and the theory of gases [English translation of La Voie lactée et la théorie des gaz], Popular Astron. **14**, 475 (1906).
[4] F. Zwicky, The redshift of extragalactic nebulae, Helv. Phys. Acta **6**, 110 (1933).
[5] F. Zwicky, Republication of: The redshift of extragalactic nebulae, Gen. Relativ. Gravit. **41**, 207 (2009).
[6] V. C. Rubin and W. K. Ford, Jr., Rotation of the andromeda nebula from a spectroscopic survey of emission regions, Astrophys. J. **159**, 379 (1970).
[7] J. Binney and S. Tremaine, *Galactic Dynamics: Second Edition*, Princeton Series in Astrophysics (Princeton University Press, Princeton, NJ, 2008).
[8] P. S. M. Persic and F. Stel, The universal rotation curve of spiral galaxies—I. The dark matter connection, Mon. Not. R. Astron. Soc. **281**, 27 (1996).
[9] L. Perivolaropoulos and F. Skara, Challenges for λCDM: An update, New Astron. Rev. **95**, 101659 (2022).

[10] V. Springel, R. Pakmor, A. Pillepich, R. Weinberger, D. Nelson, L. Hernquist, M. Vogelsberger, S. Genel, P. Torrey, F. Marinacci, and J. Naiman, First results from the IllustrisTNG simulations: Matter and galaxy clustering, Mon. Not. R. Astron. Soc. **475**, 676 (2017).
[11] T. Harko, Bose-Einstein condensation of dark matter solves the core/cusp problem, J. Cosmol. Astropart. Phys. 05 (2011) 022.
[12] V. C. Rubin, W. K. Ford, Jr., and N. Thonnard, Rotational properties of 21 SC galaxies with a large range of luminosities and radii, from NGC 4605 (R = 4 kpc) to UGC 2885 (R = 122 kpc), Astrophys. J. **238**, 471 (1980).
[13] B. Moore, S. Ghigna, F. Governato, G. Lake, T. Quinn, J. Stadel, and P. Tozzi, Dark matter substructure within galactic halos, Astrophys. J. **524**, L19 (1999).
[14] D. N. Spergel, L. Verde, H. V. Peiris, E. Komatsu, M. Nolta, C. L. Bennett, M. Halpern, G. Hinshaw, N. Jarosik, A. Kogut *et al.*, First-year Wilkinson microwave anisotropy probe (WMAP)* observations: Determination of cosmological parameters, Astrophys. J. Suppl. Ser. **148**, 175 (2003).
[15] E. Komatsu, J. Dunkley, M. Nolta, C. Bennett, B. Gold, G. Hinshaw, N. Jarosik, D. Larson, M. Limon, L. Page *et al.*, Five-year Wilkinson microwave anisotropy probe* observations: Cosmological interpretation, Astrophys. J. Suppl. Ser. **180**, 330 (2009).
[16] P. Collaboration, P. Ade, N. Aghanim, C. Armitage-Caplan, M. Arnaud *et al.*, Planck 2015 results, XIII. Cosmological parameters, Astron. Astrophys. **594**, A13 (2016).
[17] M. Lisanti, Lectures on dark matter physics, in *New Frontiers in Fields and Strings: TASI 2015 Proceedings of the 2015 Theoretical Advanced Study Institute in Elementary Particle Physics* (World Scientific, Singapore, 2017), pp. 399–446.
[18] H. Abdallah, A. Abramowski, F. Aharonian, F. A. Benkhali, E. Angüner, M. Arakawa, M. Arrieta, P. Aubert, M. Backes, A. Balzer *et al.*, Search for γ-ray line signals from dark matter annihilations in the inner galactic halo from 10 years of observations with HESS, Phys. Rev. Lett. **120**, 201101 (2018).
[19] M. Schumann, Direct detection of WIMP dark matter: Concepts and status, J. Phys. G **46**, 103003 (2019).
[20] C. Rott, Status of dark matter searches (rapporteur talk), Proc. Sci. ICRC2017 (**2017**) 1119 [arXiv:1712.00666].
[21] X. Collaboration, E. Aprile, J. Aalbers, F. Agostini, M. Alfonsi, L. Althueser, F. Amaro, M. Anthony, F. Arneodo, L. Baudis *et al.*, Dark matter search results from a one ton-year exposure of XENON1T, Phys. Rev. Lett. **121**, 111302 (2018).
[22] Z. Cao *et al.* (LHAASO Collaboration), Constraints on heavy decaying dark matter from 570 days of LHAASO observations, Phys. Rev. Lett. **129**, 261103 (2022).
[23] R. Ruffini and S. Bonazzola, Systems of self-gravitating particles in general relativity and the concept of an equation of state, Phys. Rev. **187**, 1767 (1969).
[24] P.-H. Chavanis, Mass-radius relation of Newtonian self-gravitating Bose-Einstein condensates with short-range interactions. I. Analytical results, Phys. Rev. D **84**, 043531 (2011).
[25] A. Suárez, V. H. Robles, and T. Matos, A review on the scalar field/Bose-Einstein condensate dark matter model, Astrophys. Space Sci. Proc. **38**, 107 (2014).
[26] E. J. Madarassy and V. T. Toth, Evolution and dynamical properties of Bose-Einstein condensate dark matter stars, Phys. Rev. D **91**, 044041 (2015).
[27] P.-H. Chavanis, Collapse of a self-gravitating Bose-Einstein condensate with attractive self-interaction, Phys. Rev. D **94**, 083007 (2016).
[28] L. Hui, J. P. Ostriker, S. Tremaine, and E. Witten, Ultralight scalars as cosmological dark matter, Phys. Rev. D **95**, 043541 (2017).
[29] P.-H. Chavanis, Jeans mass-radius relation of self-gravitating Bose-Einstein condensates and typical parameters of the dark matter particle, Phys. Rev. D **103**, 123551 (2021).
[30] A. K. Verma, R. Pandit, and M. E. Brachet, Formation of compact objects at finite temperatures in a dark-matter-candidate self-gravitating bosonic system, Phys. Rev. Res. **3**, L022016 (2021).
[31] A. K. Verma, R. Pandit, and M. E. Brachet, Rotating self-gravitating Bose-Einstein condensates with a crust: A model for pulsar glitches, Phys. Rev. Res. **4**, 013026 (2022).
[32] P.-H. Chavanis, Phase transitions between dilute and dense axion stars, Phys. Rev. D **98**, 023009 (2018).
[33] E. Braaten and H. Zhang, Colloquium: The physics of axion stars, Rev. Mod. Phys. **91**, 041002 (2019).
[34] P. Sikivie, Axion cosmology, in *Axions* (Springer, New York, 2008), pp. 19–50.
[35] A. M. Gavrilik and A. V. Nazarenko, Axionlike dark matter model involving two-phase structure and two-particle composites, Phys. Rev. D **108**, 123030 (2023).
[36] M. Y. Khlopov, B. A. Malomed, and Y. B. Zeldovich, Gravitational instability of scalar fields and formation of primordial black holes, Mon. Not. R. Astron. Soc. **215**, 575 (1985).
[37] This is based on the assumption [25] that the scattering length could be negative initially, to accelerate the structure formation, and later become positive to prevent complete collapse. However, the mechanism by which the sign changes remains unknown.
[38] S. Sinha, A. Y. Cherny, D. Kovrizhin, and J. Brand, Friction and diffusion of matter-wave bright solitons, Phys. Rev. Lett. **96**, 030406 (2006).
[39] L. Khaykovich and B. A. Malomed, Deviation from one dimensionality in stationary properties and collisional dynamics of matter-wave solitons, Phys. Rev. A **74**, 023607 (2006).
[40] N. G. Parker, A. M. Martin, S. L. Cornish, and C. S. Adams, Collisions of bright solitary matter waves, J. Phys. B **41**, 045303 (2008).
[41] A. M. Gavrilik, M. V. Khelashvili, and A. V. Nazarenko, Bose-Einstein condensate dark matter model with three-particle interaction and two-phase structure, Phys. Rev. D **102**, 083510 (2020).
[42] N. G. Berloff, M. Brachet, and N. P. Proukakis, Modeling quantum fluid dynamics at nonzero temperatures, Proc. Natl. Acad. Sci. U.S.A. **111**, 4675 (2014).
[43] G. Krstulovic and M. Brachet, Energy cascade with small-scale thermalization, counterflow metastability, and anomalous velocity of vortex rings in fourier-truncated Gross-Pitaevskii equation, Phys. Rev. E **83**, 066311 (2011).

[44] V. Shukla, M. Brachet, and R. Pandit, Turbulence in the two-dimensional Fourier-truncated Gross–Pitaevskii equation, New J. Phys. **15**, 113025 (2013).
[45] S. F. Shandarin and Y. B. Zeldovich, The large-scale structure of the universe: Turbulence, intermittency, structures in a self-gravitating medium, Rev. Mod. Phys. **61**, 185 (1989).
[46] V. Sahni and A. Toporensky, Cosmological hysteresis and the cyclic universe, Phys. Rev. D **85**, 123542 (2012).
[47] G. Krstulovic and M. Brachet, Energy cascade with small-scale thermalization, counterflow metastability, and anomalous velocity of vortex rings in Fourier-truncated Gross-Pitaevskii equation, Phys. Rev. E **83**, 066311 (2011).
[48] T. Y. Hou and R. Li, Computing nearly singular solutions using pseudo-spectral methods, J. Comput. Phys. **226**, 379 (2007).
[49] U. Giuriato and G. Krstulovic, Active and finite-size particles in decaying quantum turbulence at low temperature, Phys. Rev. Fluids **5**, 054608 (2020).
[50] C. Huepe, S. Métens, G. Dewel, P. Borckmans, and M. E. Brachet, Decay rates in attractive bose-einstein condensates, Phys. Rev. Lett. **82**, 1616 (1999).
[51] We can also use the SGLPE to prepare the initial condition for our binary-star study, but we use the Newton method because of it yields much faster convergence to the stationary solution of the GPPE.
[52] Y. B. Zel'Dovich, Gravitational instability: An approximate theory for large density perturbations, Astron. Astrophys. **5**, 84 (1970).
[53] M. Rao, H. Krishnamurthy, and R. Pandit, Magnetic hysteresis in two model spin systems, Phys. Rev. B **42**, 856 (1990).
[54] V. Sahni and A. Toporensky, Cosmological hysteresis and the cyclic universe, Phys. Rev. D **85**, 123542 (2012).
[55] Y. Cai, Y. Yuan, M. Rosenkranz, H. Pu, and W. Bao, Vortex patterns and the critical rotational frequency in rotating dipolar Bose-Einstein condensates, Phys. Rev. A **98**, 023610 (2018).
[56] A. Bernal and F. S. Guzmán, Scalar field dark matter: Head-on interaction between two structures, Phys. Rev. D **74**, 103002 (2006).
[57] E. Cotner, Collisional interactions between self-interacting nonrelativistic boson stars: Effective potential analysis and numerical simulations, Phys. Rev. D **94**, 063503 (2016).
[58] M. P. Hertzberg, Y. Li, and E. D. Schiappacasse, Merger of dark matter axion clumps and resonant photon emission, J. Cosmol. Astropart. Phys. 07 (2020) 067.
[59] G. Dvali, O. Kaikov, F. Kuhnel, J. S. Valbuena-Bermúdez, and M. Zantedeschi, Vortex effects in merging black holes and saturons, arXiv:2310.02288.
[60] M. P. Silverman and R. L. Mallett, Dark matter as a cosmic Bose-Einstein condensate and possible superfluid, Gen. Relativ. Gravit. **34**, 633 (2002).
[61] N. Zinner, Vortex structures in a rotating BEC dark matter component, Phys. Res. Int. **2011**, 734543 (2011).
[62] E. J. Madarassy and V. T. Toth, Numerical simulation code for self-gravitating Bose–Einstein condensates, Comput. Phys. Commun. **184**, 1339 (2013).